scientific reports

OPEN

Wafer-scale formation of MoS_2 with controlled thickness and high uniformity via conversion of MoO_x using H_2S sulfurization and subsequent crystallization

Naoya Okada[1]✉, Shinichi Tanabe[2]✉, Hitoshi Miura[2], Hao Cheng[2], Yumin Huang[2], Hisashi Warashina[2], Atsuki Fukazawa[2], Hiroki Maehara[2] & Toshifumi Irisawa[1]

Achieving uniform, high-quality, and thickness-controlled two-dimensional semiconductor films at the wafer scale remains a critical challenge for practical device integration. This work presents a scalable synthesis method for MoS_2 films on Si/SiO_2 wafers using a three-step conversion (3SC) process. The process comprises the deposition of an amorphous MoO_x film, low-temperature high-pressure H_2S annealing for sulfurization, and high-temperature Ar annealing to enhance crystallinity. Precise thickness control, from monolayer to ~20 nm, is realized by adjusting the initial MoO_x thickness. A higher oxygen content in MoO_x improves sulfurization efficiency and promotes uniform conversion to MoS_2. Structural and optical characterizations using Raman and Photoluminescence (PL) spectroscopy confirm enhanced crystallinity, with a PL-FWHM narrowed to ~0.08 eV. The 3SC method achieves uniform MoS_2 coverage across the entire wafer, demonstrating its compatibility with large-area fabrication and its potential for future electronics and optoelectronics applications.

Two-dimensional (2D) semiconductors are promising candidates for next-generation electronic and optoelectronic devices due to their atomically thin structure, excellent electronic and optical properties, and tunable bandgaps[1–3]. Moreover, 2D materials can exist as both monolayers and multilayers; precise thickness control enables further tuning of their physical and chemical properties, thereby broadening their potential applications. For example, monolayer 2D materials are well suited for transparent and flexible electronics, whereas multilayers structures are advantageous for photovoltaic applications, highlighting the importance of highly controlled thickness of 2D materials[4]. Among them, molybdenum disulfide (MoS_2) has attracted particular attention for its high carrier mobility, mechanical flexibility, and compatibility with existing semiconductor processes. These properties make MoS_2 a strong candidate for a variety of applications, including flexible electronics, photo detectors, and scaled transistors. Notably, the monolithic integration of MoS_2 thin-film transistors (TFTs) with micro-LEDs has been demonstrated using MoS_2 directly synthesized on GaN wafers, highlighting its potential for advanced optoelectronics technologies[5]. Another rapidly emerging application is the use of 2D semiconductors as alternative channel materials to silicon in complementary metal-oxide-semiconductor (CMOS) transistors for large-scale integrated circuits (LSIs)[6], where scaling limitations of conventional semiconductors are becoming increasingly significant. The 2D semiconductors offer significant advantages in overcoming the ultimate limits of CMOS miniaturization due to their high carrier mobility, which exceeds 100 $cm^2/V{\cdot}s$[7], and their extremely thin single-layer thickness of approximately 0.7 nm, providing the potential to surpass the properties of Si[7,8]. Additionally, transition metal dichalcogenides (TMDCs) have a smaller dielectric constant compared to Si (11.9), with MoS_2 and WSe_2 exhibiting values of approximately 5[9]. This lower dielectric constant helps suppress short-channel effects in transistors. Due to these attractive characteristics, many researchers have recently reported significant advancements in 2D materials for scaled CMOS transistors. For instance, transistors based on TMDCs have demonstrated a high on-current of 1.23 mA/μm with an on/off ratio exceeding 10^8, outperforming their Si CMOS counterparts[10]. Leading research institutions and companies have also actively pursued the integration of TMDCs into CMOS technology on 300-mm substrates[11–14]. A

[1]Semiconductor Frontier Research Center, National Institute of Advanced Science and Technology (AIST), Tsukuba Central 2, 1-1-1 Umezono, Tsukuba 305- 8568, Ibaraki, Japan. [2]Tokyo Electron Limited, Akasaka Biz Tower, 3-1 Akasaka 5-chome, Minato-ku, Tokyo 107-6325, Japan. ✉email: okada-naoya@aist.go.jp; shinichi.tanabe@tel.com

high on-current of 420 μA/μm has been reported on a 300-mm substrate by transferring TMDC films[15], with an expected 42% improvement in energy efficiency compared to Si devices[16]. Such research advancements will drive continued progress for CMOS scaling. Moving forward, TMDC-channel CMOS technology must focus on minimizing performance variations and improving characteristic controllability to meet the stringent requirements of advanced Si CMOS. Accordingly, realizing uniform, high-quality, and thickness-controlled TMDCs films on wafer scale remains a key challenge for practical device integration[17].

The direct growth of MoS_2 on wafers has been successfully achieved via a metal-organic chemical vapor deposition (MOCVD) process[18–20], demonstrating a variation in transistor characteristics of ~ 12.86% and an excellent yield of ~ 99.9%[19]. As another scalable synthesis method, conversion techniques involving the transformation of a metal or oxide film into a TMDC film have also been reported[21]. In this approach, a pure transition metal or transition metal oxide film is first deposited as a starting film using techniques such as sputtering[22], evaporation[23–26], pulsed laser deposition[27–29], or atomic layer deposition[30,31]. Subsequently, the deposited film is converted into TMDCs through a reaction with a chalcogen vapor, using either a solid source or chalcogen gas. In the case of MoS_2, starting films such as molybdenum (Mo) [22,24,26], epitaxial MoO_2[27–29], and amorphous Mo oxide[23,25,26,30,31] have been employed, while sulfurization or reduction sources include elemental sulfur (S)[22–29], hydrogen (H_2)[23], and hydrogen sulfide (H_2S)[30,31]. This approach holds significant potential for achieving precise thickness control, uniformity, and conformity, with these capabilities determined by the properties of the starting film. However, the material and composition of the starting film, as well as the chalcogenation conditions, have not yet been universally optimized.

In this work, we present a scalable three-step conversion (3SC) method that enables precise control over the thickness and crystallinity of MoS_2 films through the sulfurization of amorphous Mo oxide (MoO_x) under optimized processing conditions. By tuning the oxygen content of the initial MoO_x film and carefully controlling temperature and pressure during H_2S annealing, we achieve uniform MoS_2 films with precisely controlled thickness, from a monolayer to ~ 20 nm, exhibiting optical and structural properties comparable to those of single-crystalline counterparts. This process-driven approach offers a robust, reproducible, and LSI-compatible route for integrating high-quality 2D semiconductors into large-area electronic device fabrication.

Methods

First step of 3SC method

As the first step of the 3SC method, MoO_x ($x \leq 3$) films were deposited onto SiO_2/Si substrates using physical vapor deposition techniques. This deposition step is critical for accurately controlling film thickness and ensuring the high quality of the resulting MoS_2. To identify the optimal starting film, MoO_x films were prepared using electron beam evaporation (EB), ion-assisted deposition (IA), ion plating (IP), sputtering (SP), and atomic layered deposition (ALD). For the physical vapor deposition methods (EB, IA, IP, and SP), solid Mo and Mo oxide targets were employed, and O_2 gas was introduced during deposition conducted at temperatures ranging from room temperature (RT) to 150 °C. This process resulted in variations in the oxygen content (x) of the MoO_x films, enabling a systematic investigation of how the initial composition influences subsequent sulfurization and crystallization processes. The resulting MoO_x film, deposited on either a 4-inch wafer or a 10 mm × 10 mm square substrate, was then subjected to thermal annealing to facilitate MoS_2 formation via sulfurization (second step) and crystallization (third step).

Second step of 3SC method

In the second step, H_2S gas was introduced into the reactor at a pressure ranging from 0.1 to 50 kPa. Once the pressure stabilized, the substrate temperature was raised and maintained between 100 and 1000 °C. Heating was applied using lamp (manufacturer: THERMO RIKO Co., Ltd., model: GVP298, power range: 0.1–2 kW, wavelength: 700–3000 μm) positioned above the 10 mm × 10 mm square substrate, while a direct substrate heating method was used for 4-inch wafers. The heating rate was in the range of 1–10 °C/s, and variations within this range were confirmed to have no significant effect on the film quality. This H_2S annealing was carried out for 10 min to promote sulfurization, after which the H_2S gas was exhausted. Cooling proceeded naturally without rate control. Because H_2S is highly toxic, it was exhausted through an abatement system after processing. High-pressure H_2S was handled in a sealed chamber enclosed within a safety cabinet, and the laboratory is continuously monitored using gas detectors. These safety measures are commonly applied to other semiconductor process gases (e.g., SiH_4) and are therefore not unique.

Third step of 3SC method

In the third step, Ar gas was introduced into the reactor at a pressure of 60 – 100 kPa as part of a vacuum-integrated process following the second step, and the substrate temperature was further increased to 1000–1100 °C. This Ar annealing step was maintained for 10 min to enhance the crystallinity of the MoS_2 film.

Characterization of the film

As an evaluation index for MoS_2, the Raman spectroscopy has been extensively utilized and studied, particularly for single-crystalline MoS_2. In contrast, although this work focuses on polycrystalline MoS_2 synthesized via the 3SC method, the characterization of polycrystalline MoS_2 remains insufficiently explored due to the complexity introduced by grain boundaries. Accordingly, it is essential to establish a reliable evaluation index specifically for polycrystalline MoS_2 in order to efficiently advance and optimize synthesis method efficiently. Various grain boundary structures have been reported in polycrystalline MoS_2, which may induce internal stress and defects, thereby influencing its Raman spectra; particularly the disorder-related modes such as longitudinal optical (LO) and transverse optical (TO) modes[32,36]. Accordingly, we used the LO mode of 360 cm^{-1}, which exhibits relatively higher Raman intensity compared to out-of-plane optical (ZO) mode of 420 cm^{-1}, as an indicator of

polycrystalline MoS_2 film quality. Raman spectroscopy was performed on a 10 mm × 10 mm square substrate using a 488-nm continuous-wave laser with an output power of ~ 0.5 mW, focused to a spot size of ~ 2 μm in a diameter, while a 532-nm continuous-wave laser was used for in-plane mapping measurements on the 4-inch wafer. The film was further evaluated using Photoluminescence (PL) spectroscopy and X-ray photoelectron spectroscopy (XPS).

Results and discussion

Initial MoO_x film

We first explored the optimal oxygen composition x in the initial MoO_x film for the 3SC method. Raman measurements and TEM observations confirmed that the MoO_x films were in an amorphous state, regardless of the deposition methods (electron beam evaporation (EB), ion-assisted deposition (IA), ion plating (IP), sputtering (SP), and atomic layered deposition (ALD)). Each MoO_x film thickness was precisely adjusted to ~ 1–2 nm to yield a monolayer or bilayer of MoS_2 after conversion. For thicker MoS_2 films, initial MoO_x thickness corresponding to 20–30 nm were similarly prepared. These films were then converted into MoS_2 through H_2S annealing at 600 °C, followed by Ar annealing at 1100 °C to enhance crystallinity (Fig. 1a). The Raman and Photoluminescence (PL) spectra of the resulting MoS_2, converted form the MoO_x (x = 2.8) film deposited by EB, are shown in Fig. 1b,c. In the Raman spectra, both LO and ZO modes[32] were observed, indicating the presence of the disorder-related modes associated with grain boundaries. In the PL spectra, a main A peak at 1.87 eV, corresponding to a combination of the negatively charge trion (A^-) and neutral exciton (A^0) peaks, and a shoulder B peak at 2.0 eV were detected. Notably, the full width at half maximum (FWHM) of the A peak decreased with increasing MoO_3 content in the initial MoO_x film, approaching the PL-FWHM of 0.06 – 0.08 eV characteristic of single-crystalline monolayer MoS_2, as shown in Fig. 1d. Here, a single Voigt profile was used to fit the A signal, which includes both the A^0 and A^- components, for the extraction of the PL-FWHM. This approach was adopted because separating A^0 and A^- peaks becomes difficult when the PL intensity is weak, although the A^0 exciton is dominant under high PL intensity conditions, as shown in Fig. 1c. The trend in Fig. 1d indicates that the oxygen content in MoO_x plays a crucial role in determining the optical properties and overall quality of the resulting MoS_2 film. Specifically, a higher oxygen content, closer to that of MoO_3, appears to enhance the sulfurization process, enabling a more complete and uniform conversion to MoS_2.

To verify the effect of the initial MoO_x film composition on the resulting MoS_2 film, we also investigated thick films. The thick $MoO_{2.89}$ film was sulfurized to a depth of 10.7 nm from the surface, while the deeper region remained unsulfurized after H_2S annealing at 600 °C followed by Ar annealing at 1100 °C, as shown in Fig. 2a. In contrast, the thick $MoO_{2.98}$ film underwent complete sulfurization, achieving full conversion to MoS_2 across the

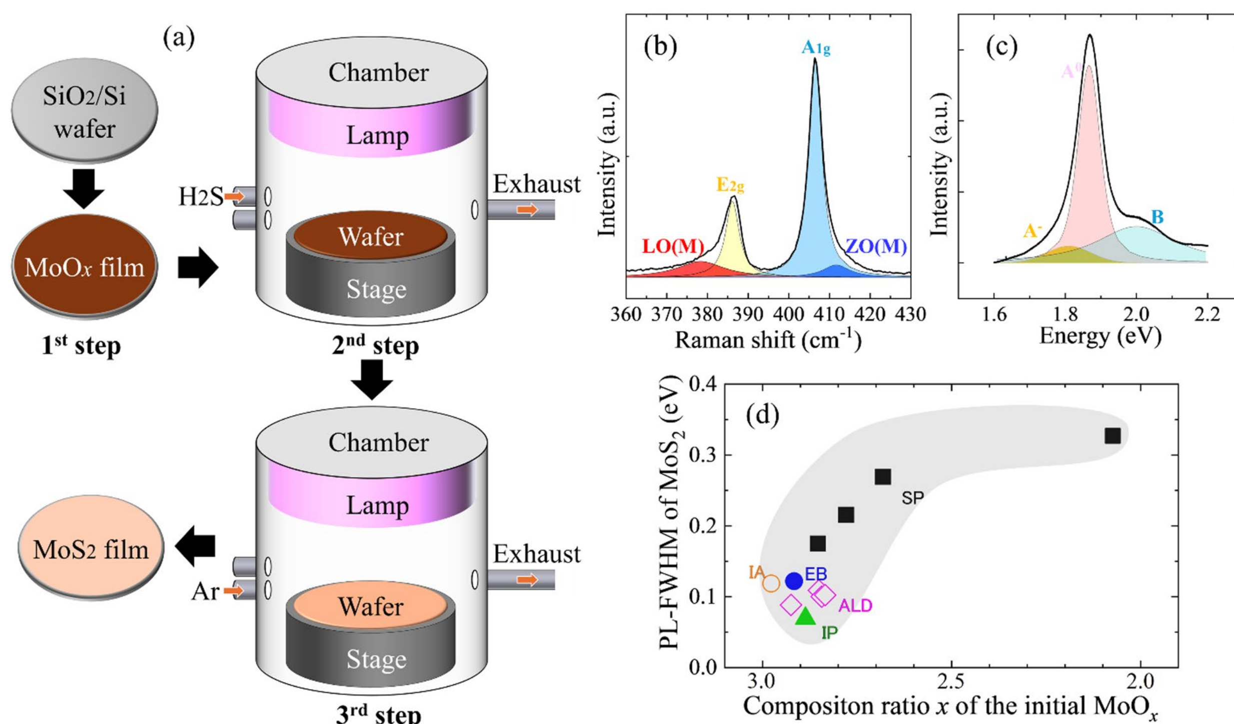

Fig. 1. (**a**) Wafer-scale growth of MoS_2 films using an annealing system based on the three-step conversion (3SC) method. (**b**) Raman and (**c**) Photoluminescence (PL) spectra of monolayer MoS_2 synthesized by the 3SC method. (**d**) Full width at half maximum (FWHM) of the PL peak of the monolayer MoS_2 synthesized by the 3SC method as a function of the composition ratio x in the initial MoO_x film, deposited using electron beam evaporation (EB), ion-assisted deposition (IA), ion plating (IP), sputtering (SP), and atomic layered deposition (ALD) methods.

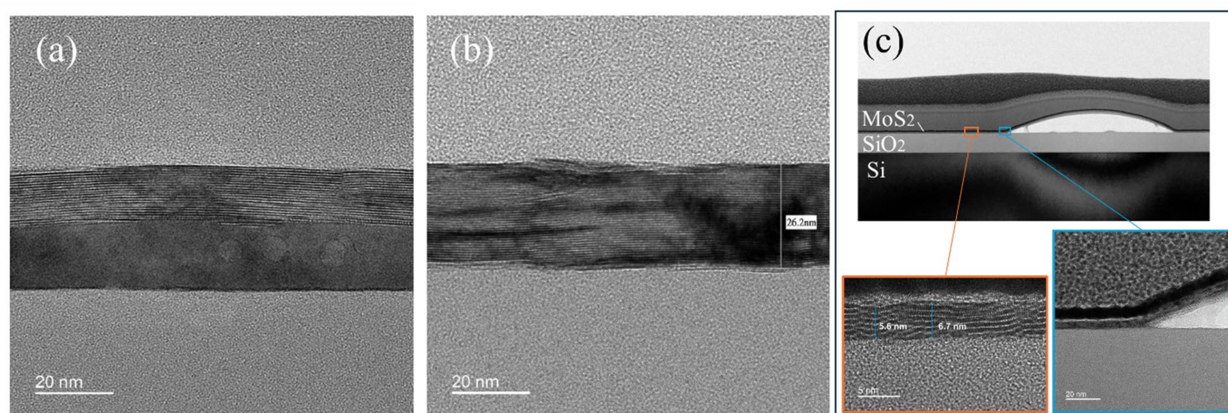

Fig. 2. Cross-sectional transmission electron microscopy (TEM) images of MoS_2 films synthesized from initial MoO_x films with (**a**) $x = 2.89$ and (**b**) $x = 2.98$, and from (**c**) a Mo film after H_2S annealing at 600 °C followed by Ar annealing at 1100 °C. (**c**) Delamination is observed in (c).

entire 26 nm thickness under the same sulfurization condition, as shown in Fig. 2b. This finding indicates that MoO_x films with higher oxygen content promote sulfurization. This behavior can be explained by considering the molar volumes of the materials involved. The molar volumes of Mo, MoO_2, MoO_3, and MoS_2 were calculated to be 9.4, 19.8, 30.7, and 31.6 cm^3/mol, respectively, based on their molecular weights (95.9, 127.9, 143.9, and 160.1 g/mol) and densities (10.2, 6.5, 4.7, and 5.1 g/cm^3). These values indicate that MoO_3 and MoS_2 possess similar molar volumes, which likely suppresses volume expansion during the conversion process. As a result, structural stability is improved, and internal stress is reduced in MoS_2 films synthesized from MoO_3. In other words, when sulfurization occurs in MoO_x with a lower oxygen content ($x < 3$), strain induced by volumetric expansion can inhibit further sulfurization reactions or the thermal diffusion of sulfide species into the MoO_x film. Additionally, we propose the following mechanism. The amorphous MoO_3 film is likely composed of molecular-scale structural units resembling the MoO_6 octahedral units found in crystalline MoO_3[33]. This structural characteristic is significant, as MoO_6 octahedra can potentially rearrange into the trigonal prismatic coordination of 2H-MoS_2 during sulfurization[34]. The presence of such prearranged structural units in the amorphous MoO_3 film may facilitate a controlled and uniform conversion, resulting in high-quality MoS_2 with fewer defects and lower residual stress. To clarify the effect of volumetric expansion during conversion to MoS_2, we also investigated Mo as an initial film. An initial Mo film with a thickness of 3.2 nm was converted into a sulfurized MoS_2 film with a thickness of 5.6 nm, corresponding to a 1.7-fold increase. This significant expansion led to the formation of wrinkles, attributed to stress induced by volume expansion during sulfurization. The internal stress generated in the MoS_2 exceeded its adhesion strength to the underlying SiO_2, ultimately causing film delamination and wrinkle formation, as shown in Fig. 2c. In contrast, MoS_2 films derived from initial MoO_x (x = 2.8) films exhibited significantly less expansion, with the sulfurized MoS_2 film showing only a 1.1-fold increase in thickness. As a result, no wrinkles were observed at this thickness, even at 20 nm, although they began to appear when the thickness reached 30 nm. These wrinkles are associated with a weak adhesion at the van der Waals interface between MoS_2 and the substrate. This comparison suggests that the initial film plays a crucial role in suppressing stress accumulation during sulfurization, thereby improving film adhesion.

Annealing conditions for conversion from MoO_x to MoS_2

To investigate the effect of the second-step H_2S annealing conditions, two types of samples were prepared under different H_2S pressure: a low pressure of 100 Pa and a high pressure of 50 kPa. The MoO_x ($x = 2.8$) film with a thickness of 0.7 nm, synthesized by EB, was used to achieve a monolayer of MoS_2. This was followed by second-step H_2S annealing at 300 °C and third-step Ar annealing at 1100 °C. Despite the H_2S pressure being the only variable, a significant difference in Raman peak intensity was observed, as shown in Fig. 3a,b. To clarify the cause of this difference, the films were analyzed using XPS before and after the H_2S annealing, as shown in Fig. 3c,d. The initial MoO_x film primarily consisted of MoO_3 (Mo^{6+}), with a minor MoO_2 (Mo^{5+}) component, as shown in Fig. 3c. After annealing under high-pressure H_2S, Mo-S bonds were clearly detected, evidenced by the appearance of Mo^{4+} 3*d* peaks at 229.3 eV and 232.5 eV, as shown inMo Fig. 3d. In contrast, after annealing under low-pressure H_2S, the MoO_3 (Mo^{6+}) species were reduced to MoO_2 (Mo^{5+}), with little to no sulfur incorporation observed. These results demonstrate that high-pressure H_2S annealing significantly enhances sulfurization efficiency.

To further clarify the effect of the second-step H_2S annealing, the dependence of the Raman peak intensity ratio of LO/E_{2g} on the H_2S annealing temperature was systematically investigated, as shown in Fig. 4a. A single-crystal monolayer of MoS_2 exhibits a LO/E_{2g} ratio of less than 0.1, with values closer to zero indicating a more ideal film. The LO/E_{2g} ratio of MoS_2 synthesized under the low-pressure (100 Pa) H_2S decreased with increasing H_2S annealing temperature, indicating a reduction in the Raman disorder mode as the annealing temperature increased. In comparison, the MoS_2 synthesized under the high-pressure H_2S (50 kPa) exhibited a lower LO/E_{2g} ratio than that obtained under the low-pressure H_2S, consistent with the XPS results confirming the effective

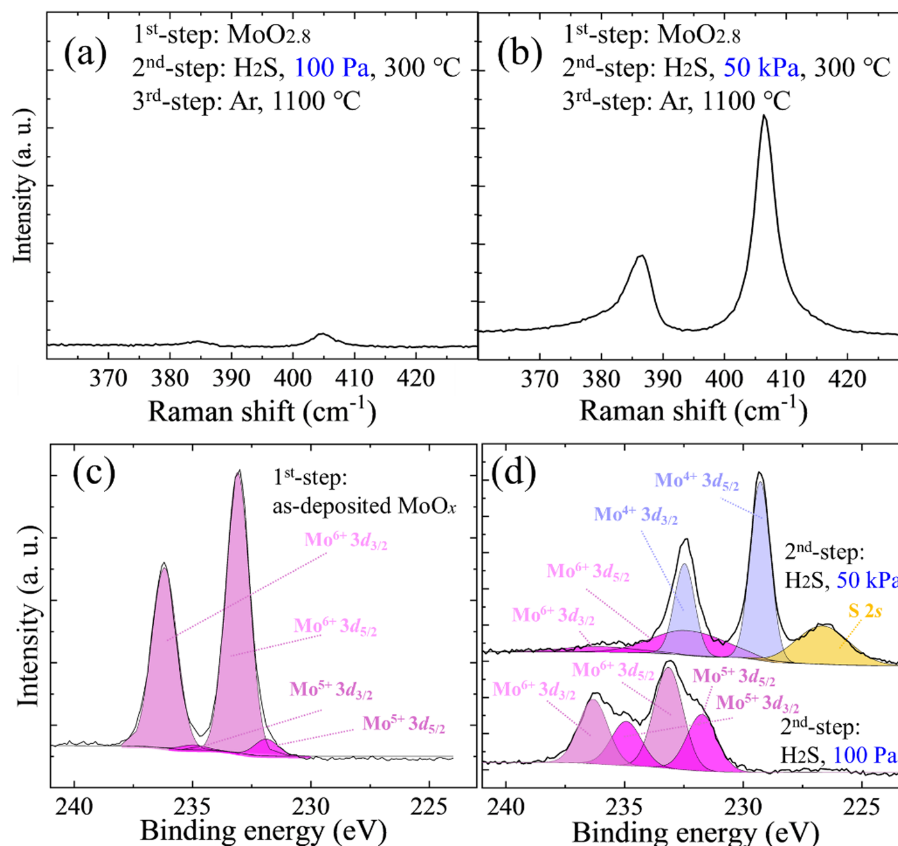

Fig. 3. Raman spectra of MoO_x films with $x = 2.8$ after H_2S annealing at 300 °C under (**a**) 100 Pa and (**b**) 50 kPa for 10 min, followed by Ar annealing at 1100 °C for 10 min. XPS spectra of (**c**) the as-deposited MoO_x films with $x = 2.8$, and (**d**) after H_2S annealing at 300 °C under 100 Pa and 50 kPa for 10 min.

sulfurization. Notably, the LO/E_{2g} ratio saturated at approximately 0.35 for annealing temperatures above 700 °C, indicating that the film quality does not further improve by H_2S annealing beyond this temperature. The H_2S annealing treatment, which involves hydrogen, may induce damage at elevated temperatures due to desulfurization-driven etching effects that generate defects in the MoS_2 film[35]. This adverse effect tends to be more pronounced in polycrystalline MoS_2, which contains numerous grain boundaries acting as reactive edge planes[36]. These edge sites are more susceptible to defect formation compared to the single-crystalline MoS_2, which is predominantly composed of chemically stable basal planes.

To overcome the limitations of the LO/E_{2g} ratio saturating at 0.35 after the second-step H_2S annealing, an Ar annealing step was introduced as a continuous third-step process. Figure 4b shows the LO/E_{2g} ratio of MoS_2 as a function of the second-step H_2S annealing temperatures, followed by a common additional Ar annealing at 1100 °C. For MoS_2 subjected to low-pressure H_2S annealing in the second step, the LO/E_{2g} ratio saturated near 0.35, even after the third-step Ar annealing. A similar saturation was observed for samples treated with high-pressure H_2S annealing above 700 °C, indicating that high-temperature H_2S exposure induces desulfurization driven etching effects, as discussed above. These effects degrade crystallinity and persist through the third step. In contrast, MoS_2 treated with high-pressure H_2S annealing below 600 °C showed a significant reduction in the LO/E_{2g} ratio to ~0.2 after the third step, closely resembling that of an ideal MoS_2 crystal. This improvement highlights the importance of low-temperature, high-pressure sulfurization conditions for achieving high crystal quality.

The third-step Ar annealing further facilitates the reconstruction of the MoS_2 crystal, leading to a reduction in grain boundary density and an increase in grain size. To visually confirm this reconstruction behavior, thick MoS_2 films were prepared before and after the third step, as shown in Fig. 4c,d. The MoS_2 subjected only to the second step exhibited a random orientation, whereas after the third step, it transformed into a well-aligned layered structure. This transformation suggests that a similar crystal reconstruction process occurs in monolayer MoS_2 during the third-step annealing. We found that the LO/E_{2g} ratio of the monolayer MoS_2 films decreases with increasing Ar annealing temperature in the range of 900–1200 °C, indicating that higher annealing temperatures help reduce structural disorder in the MoS_2 films. However, a negative shift of the A_{1g} peak was also observed with increasing annealing temperature, suggesting an increase in electron density (Fig. S1 in Supplementary information).

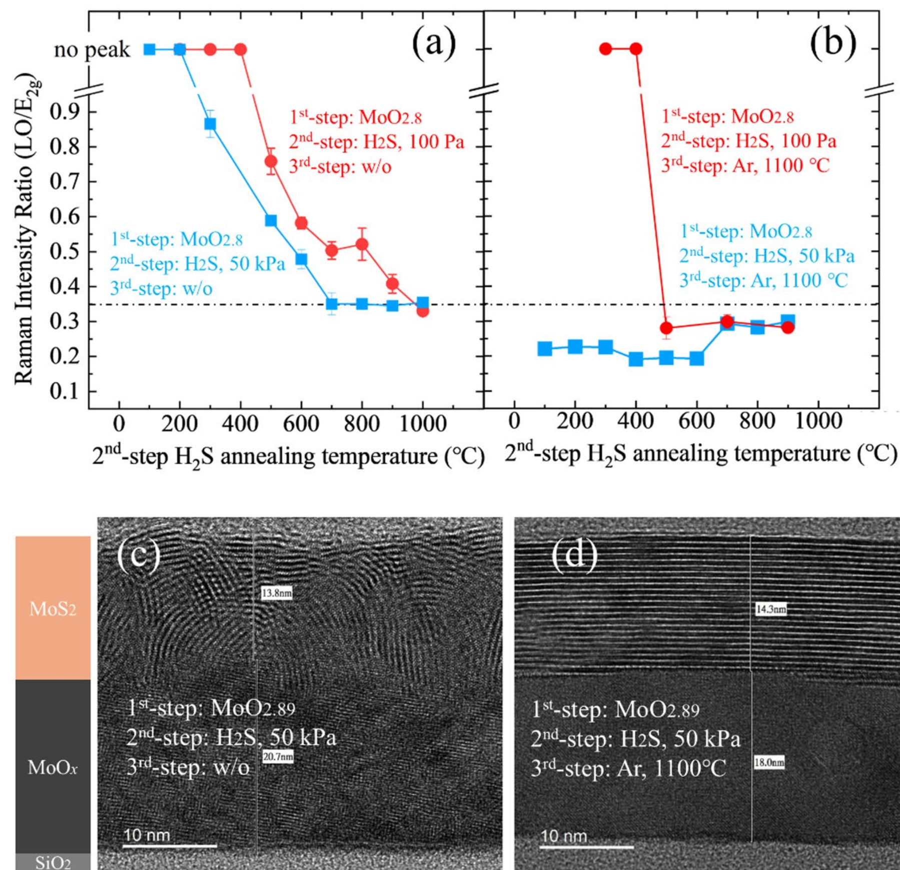

Fig. 4. Raman intensity ratio of LO/E_{2g} as a function of the H_2S annealing temperature (**a**) without and (**b**) with the following Ar annealing at 1100 °C for 10 min. MoO_x films with $x = 2.89$ were used, with H_2S annealing conducted under 100 Pa and 50 kPa for 10 min as a common condition. Cross-sectional TEM images of MoO_x films with $x = 2.89$ after H_2S annealing at 600 °C under 50 kPa for 10 min (**c**) without and (**d**) with subsequent Ar annealing at 1100 °C for 10 min.

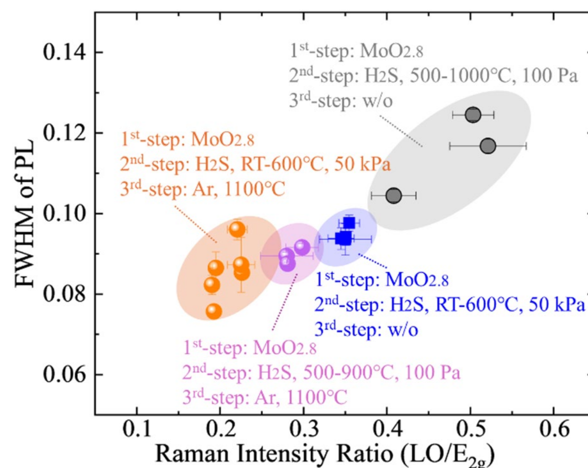

Fig. 5. FWHM of the PL peak of monolayer MoS_2 synthesized by the 3SC method under various conditions, plotted as a function of Raman intensity ratio of LO/E_{2g}.

Indicator of MoS_2 film quality

The optimized 3SC method, featuring low-temperature and high-pressure H_2S annealing in the second step followed by high-temperature Ar annealing in the third step, was established based on the observed correlation between the PL-FWHM and the Raman LO/E_{2g} intensity ratio in monolayer MoS_2 films, as shown in Fig. 5. In

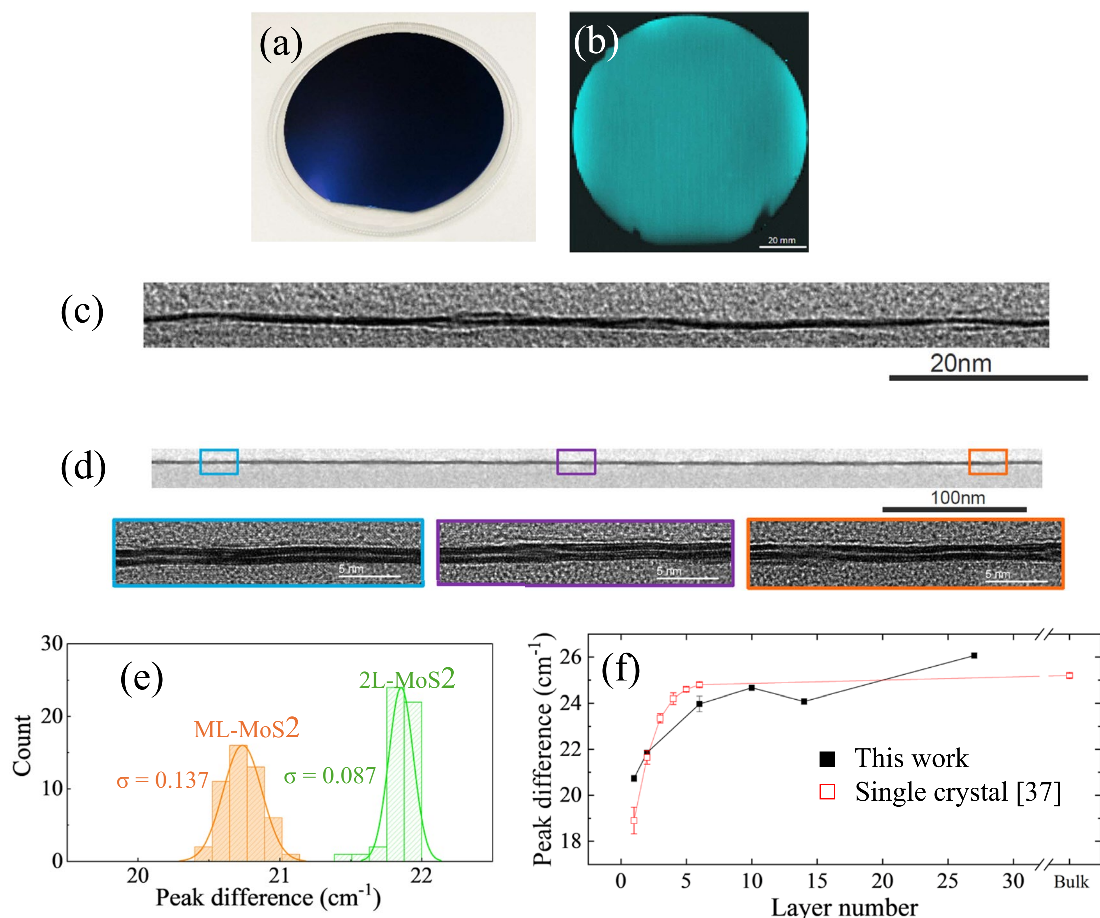

Fig. 6. (**a**) Monolayer MoS_2 film on a 4-inch Si/SiO_2 wafer synthesized by the 3SC method. (**b**) PL mapping at the exciton peak centered at 1.87 eV. Cross-sectional TEM images of (**c**) monolayer MoS_2 and (**d**) bilayer MoS_2 films on the 4-inch Si/SiO_2 wafer using the 3SC method. (**e**) Variation of Raman peak difference between the E_{2g} and A_{1g} modes at 50 points for the monolayer and bilayer MoS_2 films. (**f**) Raman peak difference between the E_{2g} and A_{1g} modes as a function of MoS_2 layer number synthesized by the 3SC method, compared to single-crystal MoS_2 data[37].

this study, a 0.7 nm-thick MoO_x ($x = 2.8$) film synthesized via EB was consistently used as the starting material. The MoS_2 films exhibited a clear relationship between the PL-FWHM and the LO/E_{2g} ratio, where lower LO/E_{2g} ratios were associated with narrower PL-FWHM values. This trend indicates that the lower-left region of Fig. 5 corresponds to an ideal single-crystalline MoS_2 film with minimal structural disorder. This correlation validates both PL-FWHM and the LO/E_{2g} ratio as complementary indicators of poly-crystalline MoS_2 film quality. Although this approach has limitations in accurately determining the grain size of MoS_2, the proposed indicators are expected to facilitate further research on poly-crystalline MoS_2 films.

Scalable synthesis of MoS_2 films

We demonstrated the scalable synthesis MoS_2 films on a 4-inch Si wafer using the 3SC method. The resulting monolayer MoS_2 film exhibited uniform and continuous coverage across the entire wafer surface, as shown in Fig. 6a. Additionally, PL mapping (Fig. 6b) validated the monolayer uniformity, revealing a strong A exciton peak centered at 1.87 eV and a narrow FWHM of ~ 0.09 eV, comparable to that of single-crystalline MoS_2. By precisely tuning the thickness of the initial MoO_x film, we achieved reliable control over the number of MoS_2 layers. Specifically, an initial MoO_x thickness of 0.7 nm yielded a monolayer MoS_2 film, while increasing the thickness to 1.2 nm resulted in a bilayer film, both with high reproducibility, as demonstrated in Fig. 6c,d. Raman spectroscopy mapping confirmed the layer uniformity, with the peak separation between the E_{2g} and A_{1g} modes showing minimal spatial variation across the wafer, as shown in Fig. 6e. Although the peak differences differed slightly from those of single-crystalline MoS_2[37], as shown in Fig. 6f, this variation is attributed to differences in strain and carrier concentration[38–42], which affect the Raman shift and reflect the polycrystalline nature of MoS_2 synthesized via the 3SC method. The grain size was estimated to be over 20 nm based on cross-sectional TEM images. The relationship between MoS_2 grain size and carrier mobility has been well reported[20,43,44], showing that films with larger grains exhibit higher mobility. For example, MoS_2 film with a typical grain size of ~ 20 nm exhibit mobilities below 0.5 $cm^2 \cdot V^{-1} \cdot s^{-1}$[43], whereas films with grain size of ~ 100 nm show mobilities as

high as 21 $cm^2 \cdot V^{-1} \cdot s^{-1}$ [120]. Accordingly, MoS_2 film synthesized using the 3SC method are expected to achieve mobilities exceeding 0.5 $cm^2 \cdot V^{-1} \cdot s^{-1}$. Larger grain sizes reduce grain-boundary-induced scattering during electron transport in the polycrystalline MoS_2 film. These characterization results demonstrate that the 3SC method enables wafer-scale production of high-quality MoS_2 films with controllable thickness and excellent optical and structural uniformity, making it a promising approach for large-area electronics and optoelectronics applications.

Conclusion

The 3SC method provides a scalable and controllable approach for synthesizing high-quality MoS_2 films on Si/SiO_2 wafers. By tuning the initial thickness of the amorphous MoO_x precursor, we achieved precise control over the resulting MoS_2 thickness, from monolayer to approximately 20 nm. The oxygen content in MoO_x was found to critically influence sulfurization efficiency and uniformity. Effective sulfur conversion was achieved via high-pressure (50 kPa), low-temperature (≤ 600 °C) H_2S annealing, followed by high-temperature (1100 °C) Ar annealing, which promoted crystal reconstruction and reduced grain boundary density. Raman and PL spectroscopy confirmed the improved structural and optical properties, with the PL FWHM of the monolayer MoS_2 narrowed to ~ 0.08 eV. Uniform MoS_2 coverage across a 4-inch wafer further demonstrated the scalability and compatibility of the process with large-area fabrication. Overall, the 3SC process provides a robust and reproducible platform for integrating 2D semiconductors into next-generation electronic and optoelectronic devices.

Data availability

The datasets generated during and/or analyzed during the current study are available from the corresponding author on reasonable request.

Received: 21 November 2025; Accepted: 29 January 2026
Published online: 05 February 2026

References

1. QH Wang KK Zadeh A Kis JN Coleman MS Strano 2012 Electronics and optoelectronics of two-dimensional transition metal dichalcogenides. *Nat. Nanotechnol.* **7** 699. https://doi.org/10.1038/NNANO.2012.193
2. AD Franklin 2015 Nanomaterials in transistors: From high-performance to thin-film applications. *Science* **349** aab2750. https://doi.org/10.1126/science.aab2750
3. M Chhowalla D Jena H Zhang 2016 Two-dimensional semiconductors for transistors. *Nat. Rev. Mater.* **1** 16052. https://doi.org/10.1038/natrevmats.2016.52
4. SJ Yun H Ko S Park BH Lee N Kim HP Duong Y Lee SM Kim KK Kim 2024 Van der Waals multilayered films: wafer-scale synthesis and applications in electronics and optoelectronics. *Adv. Funct. Mater.* **34** 2409458. https://doi.org/10.1002/adfm.202409458
5. S Hwngbo L Hu AT Hoang JY Choi J-H Ahn 2022 Wafer-scale monolithic integration of full-colour micro-LED display using MoS2 transistor. *Nat. Nanotechnol.* **17** 500. https://doi.org/10.1038/s41565-022-01102-7
6. T Irisawa 2024 Two-dimensional material transistors: Expectations observed in the IRDS road map and latest research progresses. *JSAP Rev.* https://doi.org/10.11470/jsaprev.240307
7. D Akiwande C Huyghebaert C-H Wang MI Serna S Goossens LJ Li HS Philip Wong FHL Koppens 2019 Graphene and two-dimensional materials for silicon technology. *Nature* **573** 507. https://doi.org/10.1038/s41586-019-1573-9
8. W Cao J Kang D Sarkar W Liu K Banerjee 2015 2D semiconductor FETs—projections and design for sub-10 nm. *VLSI IEEE Trans. Electron Devices* **62** 3459. https://doi.org/10.1109/TED.2015.2443039
9. Y Hou G Wang G Ma Z Feng Y Chen T Filleter 2022 Quantification of the dielectric constant of MoS2 and WSe2 Nanosheets by electrostatic force microscopy. *Mater. Charact.* **193** 112313. https://doi.org/10.1016/j.matchar.2022.112313
10. W Li X Gong Z Yu L Ma W Sun S Gao C Koroğlu 2023 Approaching the quantum limit in two-dimensional semiconductor contacts. *Nature* **613** 274. https://doi.org/10.1038/s41586-022-05431-4
11. Q Smets T Schram D Verreck D Cott B Groven Z Ahmed B Kaczer J Mitard X Wu S Kundu H Mertens D Radisic A Thiam W Li E Dupuy Z Tao K Vandersmissen T Maurice D Lin P Morin I Asselberghs I Radu 2021 Scaling of double-gated WS2 FETs to sub-5nm physical gate length fabricated in a 300mm FAB. *Int. Electron Devices Meet. (IEDM)* https://doi.org/10.1109/IEDM19574.2021.9720517
12. Q Smets D Verreck Y Shi G Arutchelvan B Groven X Wu S Sutar S Banerjee AN Mehta D Lin I Asselberghs I Radu 2020 Sources of variability in scaled MoS2 FETs. *Int. Electron Devices Meet. (IEDM)* https://doi.org/10.1109/IEDM13553.2020.9371890
13. Y Shi B Groven Q Smets S Sutar S Banerjee H Medina X Wu C Huyghebaert S Brems D Lin P Morin M Caymax I Asselberghs I Radu 2021 Superior electrostatic control in uniform monolayer MoS2 scaled transistors via in-situ surface smoothening. *Int. Electron Devices Meet. (IEDM)* https://doi.org/10.1109/IEDM19574.2021.9720676
14. S Ghosh A Kruv Q Smets T Schram DJ Leech T Ding V Turkani B Groven A Dangel G Probst T Uhrmann M Wimplinger I Asselberghs CJ Lockhart de la Rosa S Brems GS Kar 2024 Symp. EOT scaling via 300mm MX2 dry transfer - steps toward a manufacturable process development and device integration. *VLSI Technol.* https://doi.org/10.1109/VLSITechnologyandCir46783.2024.10631364
15. X Wu D Cott Z Lin Y Shi B Groven P Morin D Verreck Q Smets H Medina S Sutar I Asselberghs I Radu D Lin 2021 Dual gate synthetic MoS2 MOSFETs with 4.56µF/cm2 channel capacitance, 320µS/µm Gm and 420 µA/µm Id at 1V Vd/100nm Lg. *Int. Electron Devices Meet. (IEDM)* https://doi.org/10.1109/IEDM19574.2021.9720695
16. Z Ahmed 2020 Introducing 2D-FETs in device scaling roadmap using DTCO. *Int. Electron Devices Meet. (IEDM)* https://doi.org/10.1109/IEDM13553.2020.9371906
17. X Xu T Guo H Kim MK Hota RS Alsaadi M Lanza X Zhang HN Alshareef 2022 Growth of 2D materials at the wafer scale. *Adv. Mater.* **34** 2108258. https://doi.org/10.1002/adma.202108258
18. K Kang S Xie L Huang Y Han PY Huang KF Mak C-J Kim D Muller J Park 2015 High-mobility three-atom-thick semiconducting films with wafer-scale homogeneity. *Nature* **620** 656. https://doi.org/10.1038/nature14417
19. SS Kim S Seo J Kwon D Lee C Kim J Ryu J Kim 2024 Growth-based monolithic 3D integration of single-crystal 2D semiconductors. *Nature* **636** 615. https://doi.org/10.1038/s41586-024-08236-9
21. J Kwon M Seol J Yoo H Ryu D Ko M Lee 2024 200-mm-wafer-scale integration of polycrystalline molybdenum disulfide transistors. *Nat. Electron.* **7** 356. https://doi.org/10.1038/s41928-024-01158-4

21. M Altvater C Muratore M Snure NR Glavin 2024 Two-step conversion of metal and metal oxide precursor films to 2D transition metal dichalcogenides and heterostructures. *Small* https://doi.org/10.1002/smll.202400463
22. N Choudhary J Park JY Hwang W Choi 2014 Growth of large-scale and thickness-modulated MoS2 nanosheets. *ACS Appl. Mater.* **6** 21215. https://doi.org/10.1021/am506198b
23. Y-C Lin W Zhang J-K Huang K-K Liu Y-H Lee C-T Liang C-W Chu L-J Li 2012 Wafer-scale MoS2 thin layers prepared by MoO3 sulfurization. *Nanoscale* **4** 6637. https://doi.org/10.1039/C2NR31833D
24. Y Zhan Z Liu S Najmaei PM Ajayan J Lou 2012 Large-area vapor-phase growth and characterization of MoS2 atomic layers on a SiO2 substrate. *Small* **8** 966. https://doi.org/10.1002/smll.201102654
25. SN Heo Y Ishiguro R Hayakawa T Chikyow Y Wakayama 2016 Perspective: Highly ordered MoS2 thin films grown by multi-step chemical vapor deposition process. *APL Mater.* **4** 030901. https://doi.org/10.1063/1.4943288
26. S Fatima Y Gu SJ Yang S Kutagulla S Rizwan D Akinwande 2023 Comparative study between sulfurized MoS2 from molybdenum and molybdenum trioxide precursors for thin-film device applications. *ACS Appl. Mater.* **15** 16308. https://doi.org/10.1021/acsami.3c00824
27. X Xu Z Wang S Lopatin MAQ Lopez HN Alshareef 2019 Wafer scale quasi single crystalline MoS2 realized by epitaxial phase conversion. *2D Mater.* **6** 015030. https://doi.org/10.1088/2053-1583/aaf3e9
28. X Xu G Das X He MN Hedhili ED Fabrizio X Zhang HN Alshareef 2019 High-performance monolayer MoS2 films at the wafer scale by two-step growth. *Adv. Funct. Mater.* **29** 1901070. https://doi.org/10.1002/adfm.201901070
29. X Xu C Zhang MK Hota Z Liu Z Zhang HN Alshareef 2020 Enhanced quality of wafer-scale MoS2 films by a capping layer annealing process. *Adv. Funct. Mater.* **30** 1908040. https://doi.org/10.1002/adfm.201908040
30. R Mahlouji Y Zhang MA Verheijen JP Hofmann WMM Kessels AA Sagade AA Bol 2021 On the contact optimization of ALD-based MoS2 FETs: correlation of processing conditions and interface chemistry with device electrical performance. *ACS Appl. Mater.* **3** 3185. https://doi.org/10.1021/acsaelm.1c00379
31. N Aspiotis K Morgan B Marz 2023 Large-area synthesis of high electrical performance MoS2 by a commercially scalable atomic layer deposition process. *npj 2D Mater. Appl.* **7** 18. https://doi.org/10.1038/s41699-023-00379-z
32. AJ Mignuzzi N Pollard B Bonini IS Brennan MA Gilmore D Pimenta D Richards 2015 Effect of disorder on Raman scattering of single-layer MoS_2. *Phy. Rev. B* **91** 195411. https://doi.org/10.1103/PhysRevB.91.195411
33. IA Castro RS Datta JZ Ou AC Gomez S Sriram T Daeneke K Kalantar-Zadeh 2017 Molybdenum oxides – from fundamentals to functionality. *Adv. Mat.* **29** 1701619. https://doi.org/10.1002/adma.201701619
34. Th Weber JC Muijsers JHC Wolput van CPJ Verhagen JW Niemantsverdriet 1996 Basic Reaction steps in the sulfidation of crystalline MoO3 to MoS2, as studied by X-ray photoelectron and infrared emission spectroscopy. *J. Phys. Chem.* **100** 14144. https://doi.org/10.1021/jp961204y
35. Y Chen Z Li Y Xie B Zou Y Zu Y Zhou J Yang H Sun 2025 Strain- and Ar/H2 annealing-induced sulfur defects in monolayer MoS2 probed by Raman spectroscopy. *J. Phys. Chem. C* **129** 3145. https://doi.org/10.1021/acs.jpcc.5c00296
36. B Mortazavi R Quey A Ostadhossein A Villani N Moulin ACT Duin van T Rabczuk 2017 Strong thermal transport along polycrystalline transition metal dichalcogenides revealed by multiscale modeling for MoS2. *Appl. Mat. Today* **7** 37. https://doi.org/10.1016/j.apmt.2017.02.005
37. C Lee H Yan LE Brus TF Heinz J Hone S Ryu 2010 Anomalous lattice vibrations of single- and few-layer MoS2. *ACS Nano* **4** 2695. https://doi.org/10.1021/nn1003937
38. C Rice RJ Young R Zan U Bangert D Wolverson T Georgiou R Jalil KS Novoselov 2013 Raman-scattering measurements and first-principles calculations of strain-induced phonon shifts in monolayer MoS2. *Phys. Rev. B* **87** 081307(R). https://doi.org/10.1103/PhysRevB.87.081307
39. N Michail J Delikoukos C Parthenios K Gailotis 2016 Papagelis, Optical detection of strain and doping inhomogeneities in single layer MoS2A. *Appl. Phys. Lett.* **108** 173102. https://doi.org/10.1063/1.4948357
40. B Chakraborty A Bera DVS Muthu S Bhowmick UV Waghmare AK Sood 2012 Symmetry-dependent phonon renormalization in monolayer MoS2 transistor. *Phys. Rev. B* **85** 161403(R). https://doi.org/10.1103/PhysRevB.85.161403
41. GH Ahn M Amani H Rasool D-H Lien JP Mastandrea JW Ager III M Dubey DC Chrzan AM Minor A Javey 2017 Strain-engineered growth of two-dimensional materials. *Nat. Commun.* **8** 608. https://doi.org/10.1038/s41467-017-00516-5
42. M Okada Y Okigawa T Kubo H Nakajima T Yamada 2025 Strain engineering of MoS2 by tuning the transfer process. *ACS Appl. Mater.* **7** 3590. https://doi.org/10.1021/acsaelm.5c00467
43. J Zhang H Yu W Chen X Tian D Liu M Cheng G Xie W Yang R Yang X Bai D Shi G Zhang 2014 Scalable growth of high-quality polycrystalline MoS2 monolayers on SiO2 with tunable grain sizes. *ACS Nano* **8** 6024. https://doi.org/10.1021/nn5020819
44. DH Lee Y Sim J Wang S-Y Kwon 2020 Metal–organic chemical vapor deposition of 2D van der Waals materials—The challenges and the extensive future opportunities. *APL Mater.* **8** 030901. https://doi.org/10.1063/1.5142601

Author contributions

N. O., S. T., Y. H., C. H., H. W., and H. M. planned and conducted experiments and analyses. T. I., A. F., and H. M supervised the overall project. The manuscript was written by N. O. with contributions from all authors through discussion.

Funding

This work is based on results obtained from the project, "Research and Development Project of the Enhanced Infrastructures for Post 5G Information and Communication Systems" (JPNP20017), subsidized by the New Energy and Industrial Technology Development Organization (NEDO).

Declarations

Competing interests

The authors declare no competing interests.

Additional information

Supplementary Information The online version contains supplementary material available at https://doi.org/10.1038/s41598-026-38161-y.

Correspondence and requests for materials should be addressed to N.O. or S.T.

Reprints and permissions information is available at www.nature.com/reprints.

Publisher's note Springer Nature remains neutral with regard to jurisdictional claims in published maps and institutional affiliations.

Open Access This article is licensed under a Creative Commons Attribution-NonCommercial-NoDerivatives 4.0 International License, which permits any non-commercial use, sharing, distribution and reproduction in any medium or format, as long as you give appropriate credit to the original author(s) and the source, provide a link to the Creative Commons licence, and indicate if you modified the licensed material. You do not have permission under this licence to share adapted material derived from this article or parts of it. The images or other third party material in this article are included in the article's Creative Commons licence, unless indicated otherwise in a credit line to the material. If material is not included in the article's Creative Commons licence and your intended use is not permitted by statutory regulation or exceeds the permitted use, you will need to obtain permission directly from the copyright holder. To view a copy of this licence, visit http://creativecommons.org/licenses/by-nc-nd/4.0/.

© The Author(s) 2026